

Global navigation satellite system spoofing-detection technique based on the Doppler ripple caused by vertical reciprocating motion

He Li¹, Li Hong¹ , Lu Mingquan¹

¹Department of Electronic Engineering, Tsinghua University, Beijing 100084, People's Republic of China

 E-mail: lihongee@tsinghua.edu.cn

Abstract: The menace of spoofing is overshadowing the civilian use of the global satellite navigation system. Many anti-spoofing approaches have been intensively researched in the literature, among which the spoofing-detection ones are the most thoroughly investigated. In this study, the authors propose a novel spoofing-detection method, which jointly utilises the carrier Doppler frequency caused by the vertical reciprocating motion of the receiving antenna and the navigational information conveyed by the received signals. This specific motion pattern would make the Doppler measurement of each signal fluctuate like water ripples, of which the amplitude should be proportional to the sine of the corresponding satellite's elevation. Singular value decomposition is deployed to simultaneously estimate the speed variation of the receiving antenna and the relative amplitudes of the Doppler fluctuations. Then, the proportionality between relative amplitudes and the elevation sines is checked to detect the spoofing signal, which would probably break the proportionality. The proposed method is experimentally verified and validated. They also analyse the detection performance both theoretically and numerically. Moreover, several motion deviations are assessed both theoretically and practically.

1 Introduction

Global navigation satellite system (GNSS) has already become an indispensable infrastructure in a variety of civilian applications such as transportation, power management, and geodesy. It could provide all-time all-weather positioning, navigation, and timing services to billions of users, while only occupies a rather narrow frequency band at a considerably low power level. However, two major security defects haunt the widespread applications of the civilian GNSS. The first drawback concerns with the open access of the signal structure and characteristics, making it very easy to counterfeit the signal. The second weakness is that the signal reaching user receivers is very dim, thus making the accidental and intentional wireless interference a significant threat.

According to their functioning principles, intentional interferences can be categorised into two different types: jamming and spoofing. Jamming utilises the noise or structured interference with quite large power to deny the victim's normal reception and processing of the GNSS signal. Nonetheless, this brute-force measure is just as blatant as effective, which alerts the victim and thus prevents further damage. Unlike jamming measure, spoofing is much more sophisticated. GNSS spoofing technique usually counterfeits the GNSS signal and transmits the fake signal to the victim receiver at a reasonable power level, along with some deliberate alterations of the navigational information (ephemeris data and/or pseudorange measurements). Owing to the similarity between the spoofing signal and the authentic GNSS signal, the victim receiver might just receive and process the spoofing one without awareness, leading to a false positioning and timing solution.

The state-of-the-art spoofing technique achieves the spoofing purpose through a so-called 'lift-off' process [1]. Intensive works have been dedicated to spoofing-detection tasks, which lay the foundation of the anti-spoofing task pyramid. A comprehensive review of various spoofing strategies and a variety of spoofing-detection techniques is presented by Psiaki and Humphreys [2].

These GNSS spoofing-detection methods can be classified into three types: signal structure renovations [3, 4], external facilities such as inertial measurement unit [5, 6] and user receiver processing. Renovating the current GNSS signal to a spoof-proof one is very time-consuming and expensive. Since it calls for

replacing the present satellite constellation and upgrading numerous commercial off-the-shelf receivers. The assistance from external devices usually needs hardware redesign and incurs an extra cost. Comparatively, the signal processing-based methods only require software upgrades at a low cost. Amongst this type of spoofing-detection approaches, the single-antenna-based ones are principally simpler and more economically desirable than those based on the phased array antenna and multiple antennas or users [7–10].

Many previous works presume that the spatial diversity, which characterises the authentic GNSS signal, is absent in the spoofing signal [11–14]. In other words, they assume that the spoofing signal is transmitted from one spoofing antenna. Thus, antenna motion makes the spatial features variate differently from satellite to satellite in non-spoofing situations, while the patterns of the spoofing signals are almost identical. The variation of the Doppler or channel gain of the spoofing signal is assumed to be highly correlated, and it is monitored to detect spoofing signal [11]. Another method incorporates the antenna motion data with the carrier phase measurement to check the bearing of each signal source [12]. Another method deploys a rotating platform with a tilted receiving antenna to check if the signal amplitude variations are correlated or not [13]. The spoofing-detection method in [14] utilises the Doppler frequency difference (DFD) measurement on a rapidly moving receiver, which is usually non-linear in the non-spoofing environment, and becomes linear when there are spoofing signals.

However, the single spoofing antenna assumption, which these methods rely on, makes them ineffective against spoofs with multiple distributed transmitters. This is because these methods only utilise the presence or absence of spatial diversity, which is only a basic aspect of the spatial feature. The actual spatial feature is determined by the geometry between the receiver and the actual signal sources, which could be either the satellite constellation or the spoofing transmitter(s). The spatial signatures of authentic signals in non-spoofing scenarios corroborate with the authentic navigation solution, while in spoofing scenarios the spatial features probably disagree with the spoofed positioning result.

In this paper, we propose a spoofing-detection approach based on the Doppler variation induced by the vertical reciprocating motion of the receiving antenna. The amplitude of the consequent

ripple-like Doppler variation is proportional to the sine value of the transmitter's actual elevation. Singular value decomposition (SVD) is deployed to simultaneously estimate the relative amplitudes and the speed variation. When free of the spoofing signal, the estimated relative amplitudes are proportional to the sine values of satellite elevations derived from the positioning solution, which reflects the actual altitude of the satellites quite precisely. The authentic signals transmitted from the GNSS satellites naturally hold this consistency because of the continuous monitor and control of the ground segment. However, it is difficult for spoofers to counterfeit this consistency. When some or all of the signals are emitted from the spoofing transmitter, this consistency breaks because the actual elevation of the spoiler is probably different from the elevation presented by the navigational information.

The proposed method utilises both the signal spatial characteristic and the navigational information conveyed by the GNSS signal, which endows it the potential to detect the spoofing signal emitted from multi-antenna spoiler. Additionally, our proposed method requires no external speedometer or inertial navigation device but only some mechanism to keep the antenna motion along the vertical axis. The competent mechanism includes, but not limited to the human gravity perception by visual and vestibular sensations, a mechanical platform with the ability to make a vertical reciprocating motion or even the pitch motion of marine vehicles induced by water waves.

The remainder of this paper is organised as follows. The second chapter presents the system and signal models. The spoofing-detection method is proposed in the third chapter. In the fourth chapter, we investigate the detection performance and several impact factors either quantitatively or qualitatively. The fifth chapter includes a series of experimental results under both non-spoofing and spoofing situations. The final chapter concludes this paper with some discussion.

2 System model

The Doppler frequency measurement of the tracked signal from the i th satellite consists of four different parts

$$f_{\text{obs}}^{(i)} = f_s^{(i)} + f_u^{(i)} + \Delta f_s^{(i)} + \Delta f_u^{(i)}$$

where $f_s^{(i)}$ and $f_u^{(i)}$, respectively, represent the Doppler terms caused by the motion of the satellite and the user receiver, and $\Delta f_s^{(i)}$ and $\Delta f_u^{(i)}$ are the clock drifts of the i th satellite and the user receiver, respectively. These motion-induced Doppler terms can be modelled as follows:

$$f_s^{(i)} = -\frac{f_c}{c} (\mathbf{l}^{(i)})^T \cdot \mathbf{v}^{(i)} \quad (1)$$

$$f_u^{(i)} = \frac{f_c}{c} (\mathbf{l}^{(i)})^T \cdot \mathbf{v}_u \quad (2)$$

Here, f_c is the carrier frequency and c is the speed of light; $\mathbf{l}^{(i)}$ is the steering vector pointing from the user receiver to the i th satellite; $\mathbf{v}^{(i)}$ and \mathbf{v}_u are the velocity vectors of the i th satellite and user receiver, respectively. For a static or uniformly translating receiver, the Doppler terms $f_s^{(i)}$, $\Delta f_s^{(i)}$, and $\Delta f_u^{(i)}$ usually vary at a very slow rate. Thus, for a short interval such as 10 s, these terms change largely about 1–2 Hz. However, the Doppler term $f_u^{(i)}$ could be over 5 Hz even if the speed of the antenna motion is only 1 m/s for global positioning system (GPS) L1 signal. Therefore, in this paper, we assume that the Doppler variation induced by the vertical motion is dominant, while the other terms could be largely eliminated by averaging.

Therefore, we could focus on the motion-induced Doppler term $f_u^{(i)}$. In the local Cartesian coordinates, called East–North–up coordinate (ENU), the steering vector could be expressed as

$$\mathbf{l}^{(i)} = [\sin \varphi_i \cos \theta_i, \cos \varphi_i \cos \theta_i, \sin \theta_i] \quad (3)$$

where θ_i and φ_i are, respectively, the elevation and the azimuth from the North direction of the i th satellite. The Doppler induced by user motion could be formulated as

$$f_u^{(i)} = \frac{f_c}{c} (v_{u,x} \sin \varphi_i \cos \theta_i + v_{u,y} \cos \varphi_i \cos \theta_i + v_{u,z} \sin \theta_i) \quad (4)$$

Here, $v_{u,x}$, $v_{u,y}$ and $v_{u,z}$ are the projections of the user velocity \mathbf{v}_u on the three axes of ENU coordinate. As for the vertical motion we focus on in this paper, the first two elements in \mathbf{v}_u are zeros. Therefore, by simplifying the up-axis speed $v_{u,z}$ as v , we can express the motion-induced Doppler term as

$$f_u^{(i)} = \frac{f_c}{c} v \sin \theta_i \quad (5)$$

This simplified formulation facilitates further vectorisation. For brevity, we term this Doppler measurement caused by the user vertical reciprocating motion as the Doppler ripple, because of its ripple-like shape. The Doppler-ripple measurement of the i th satellites at the moment n can be expressed as

$$\hat{f}_u^{(i)}[n] = \frac{f_c}{c} v_n \sin \theta_i + z^{(i)}[n] \quad (6)$$

where $n = 1, 2, \dots, N$, $i = 1, 2, \dots, I$ and $z^{(i)}[n]$ is the noise term containing the thermal noise and tropospheric and ionospheric delay rates. In a short interval, $z^{(i)}[n]$ approximately obeys a zero-mean Gaussian distribution with a variance of δ_i^2 .

Pack the temporal sequence of the i th Doppler-ripple measurements into a vector as

$$\hat{\mathbf{f}}_u^{(i)} = \left[\hat{f}_u^{(i)}[1], \hat{f}_u^{(i)}[2], \dots, \hat{f}_u^{(i)}[N] \right] = \frac{f_c}{c} \sin \theta_i \mathbf{v} + \mathbf{z}^{(i)} \quad (7)$$

where the vector $\mathbf{v} = [v_1, v_2, \dots, v_N]^T$ represents the speed function of the user receiver's vertical reciprocating motion and $\mathbf{z}^{(i)} = [z^{(i)}[1], z^{(i)}[2], \dots, z^{(i)}[N]]^T$ is the corresponding noise vector.

We could further vertically pile the measurement row vector in (7) of all satellites into a matrix like

$$\hat{\mathbf{F}} = \left[\hat{\mathbf{f}}_u^{(1)}, \hat{\mathbf{f}}_u^{(2)}, \dots, \hat{\mathbf{f}}_u^{(I)} \right]^T = \frac{f_c}{c} \boldsymbol{\theta} \mathbf{v}^T + \mathbf{Z} \quad (8)$$

where the vector $\boldsymbol{\theta} = [\sin \theta_1, \sin \theta_2, \dots, \sin \theta_I]^T$ stands for the elevation sines, which remains stable in a short interval, and $\mathbf{Z} = [\mathbf{z}^{(1)}, \mathbf{z}^{(2)}, \dots, \mathbf{z}^{(I)}]^T$ is the corresponding noise matrix.

Additionally, we could denote the noiseless Doppler-ripple data as \mathbf{F} for the sake of further analysis, and it could be formulated into the form like

$$\mathbf{F} = \frac{f_c}{c} \|\boldsymbol{\theta}\| \|\mathbf{v}\| \frac{\boldsymbol{\theta}}{\|\boldsymbol{\theta}\|} \frac{\mathbf{v}^T}{\|\mathbf{v}\|} = \sigma_1 \mathbf{u}_1 \mathbf{w}_1^T \quad (9)$$

where $\sigma_1 = \frac{f_c}{c} \|\boldsymbol{\theta}\| \|\mathbf{v}\|$, $\mathbf{u}_1 = \frac{\boldsymbol{\theta}}{\|\boldsymbol{\theta}\|}$ and $\mathbf{w}_1 = \frac{\mathbf{v}}{\|\mathbf{v}\|}$. Since \mathbf{F} is the outer product of two vectors $\boldsymbol{\theta}$ and \mathbf{v} , therefore, its rank is 1.

3 Proposed method

In this chapter, we first physically explain the SVD of the Doppler ripple. Then, we exhibit the consistency between the SVD outcome of the Doppler ripple and the satellite elevation calculated from navigational information. Finally, we propose a spoofing-detection method based on the presented consistency.

3.1 SVD of Doppler-ripple measurements

In this section, we would discuss the SVD of the Doppler ripple of the authentic signals. SVD is a famous mathematical technique

widely used in various domains [15] such as communications [16] and quantum physics [17]. The SVD definition and other pertinent details are extensively investigated in many classical works.

If the measurement noise is much smaller than the pure Doppler ripple, the noisy measurement matrix $\hat{\mathbf{F}}$ in (8) could be approximated by the first singular value and vectors

$$\hat{\mathbf{F}} = \hat{\mathbf{U}}\hat{\mathbf{S}}\hat{\mathbf{W}}^T = \Sigma_{i=1}^I \hat{\sigma}_i \hat{\mathbf{u}}_i \hat{\mathbf{w}}_i^T \simeq \hat{\sigma}_1 \hat{\mathbf{u}}_1 \hat{\mathbf{w}}_1^T \quad (10)$$

In the matrix analysis terminology, $\hat{\mathbf{U}}$ is called the left singular vector matrix, of which each column vector $\hat{\mathbf{u}}_i$ is called the left singular vector. Similarly, $\hat{\mathbf{W}}$ is the consequent right singular vector matrix, whose column vector $\hat{\mathbf{w}}_i$ is called the right singular vector. $\hat{\mathbf{S}} = [\hat{\mathbf{S}}_1 \ \mathbf{O}]$ is a rectangular diagonal matrix, consisting of the singular values $\hat{\mathbf{S}}_1 = \text{diag}[\hat{\sigma}_1, \hat{\sigma}_2, \dots, \hat{\sigma}_I]$ and a zero matrix \mathbf{O} . Each $\hat{\sigma}_i$ is called the singular value and

$$\hat{\sigma}_1 \geq \hat{\sigma}_2 \geq \dots \geq \hat{\sigma}_I > 0 \quad (11)$$

Since \mathbf{F} has the rank of 1, according to the matrix theory, we could know the following facts about the noisy measurement matrix $\hat{\mathbf{F}}$:

(i) The first singular value is much larger than the other following values:

$$\hat{\sigma}_1 \simeq \frac{f_c}{c} \|\boldsymbol{\theta}\| \|\mathbf{v}\| \gg \hat{\sigma}_2 \quad (12)$$

(ii) The first right singular vector $\hat{\mathbf{w}}_1$ is approximately equal to the orthonormal base \mathbf{w}_1 in the column space of \mathbf{F} , which is spanned by \mathbf{v}

$$\text{Span}(\hat{\mathbf{w}}_1) \simeq \text{Span}(\mathbf{w}_1) = \text{Col}(\mathbf{F}) = \text{Span}(\mathbf{v}) \quad (13)$$

1. iii) The first left singular vector $\hat{\mathbf{u}}_1$ is approximately equal to the orthonormal base \mathbf{u}_1 in the row space of \mathbf{F} , which is spanned by $\boldsymbol{\theta}$

$$\text{Span}(\hat{\mathbf{u}}_1) \simeq \text{Span}(\mathbf{u}_1) = \text{Row}(\mathbf{F}) = \text{Span}(\boldsymbol{\theta}) \quad (14)$$

Since the column space of \mathbf{F} is one-dimensional and both \mathbf{w}_1 and \mathbf{v} lie within it, thus $\hat{\mathbf{w}}_1$ is a precise approximation of the vertical speed vector \mathbf{v} . The same happens to $\hat{\mathbf{u}}_1$ and $\boldsymbol{\theta}$. The single dimensionality of the row space of \mathbf{F} ensures that $\hat{\mathbf{u}}_1$ should be largely proportional to the sine value of the elevation $\boldsymbol{\theta}$.

Thus, it can be known that: (i) $\hat{\mathbf{w}}_1$ contains the temporal feature of the Doppler ripples, reflecting the speed variation of the vertical motion; (ii) $\hat{\mathbf{u}}_1$ represents the relative amplitude of each channel, containing the knowledge of geometry and the vertical motion projection on the steering vector; moreover, (iii) $\hat{\sigma}_1$ stands for the intensity of all the corresponding amounts. In the light of these facts, we would name $\hat{\mathbf{w}}_1$ as the speed vector and $\hat{\mathbf{u}}_1$ as the projection vector.

Summarily, by making a vertical reciprocating motion and accumulating the consequent Doppler-ripple measurements, and calculating the SVD, we could get a unitary vector $\hat{\mathbf{u}}_1$, which is proportional to the sine value of the actual elevation $\boldsymbol{\theta}$.

Although we present with the original SVD, another noise pre-whitening version shown in [15] is adopted in practise to improve the estimation accuracy. Before we perform SVD on $\hat{\mathbf{F}}$, a matrix \mathbf{C} , which is termed as the pre-whitening matrix, is multiplied to whiten the noise. \mathbf{C} has each diagonal element inverse to the standard deviation of the carrier Doppler measurement noise δ_i . Since the frequency error in the carrier tracking loop is well-studied, δ_i can be roughly estimated using the carrier-to-noise ratio [18]. Thus, the original SVD of $\hat{\mathbf{F}}$ transform into the weighted form as

$$\hat{\mathbf{u}}_1 = \mathbf{C}^{-1} \text{LSVD}(\hat{\mathbf{C}}\hat{\mathbf{F}}) \quad (15)$$

where Left singular vector of Singular Value Decomposition (LSVD) is the calculation of the first column of the left singular matrix. Next, we will develop a spoofing-detection method based on the projection vector $\hat{\mathbf{u}}_1$.

3.2 Consistency between the projection vector and the navigational information

In the traditional navigation process, the elevation of each satellite could be derived from the pseudorandom code and ephemeris data. We denote the sine values of the elevation angle obtained from the navigational information as $\bar{\boldsymbol{\theta}}$.

In non-spoofing scenarios, all used signals are transmitted from the authentic satellites, which sit in the positions claimed by the conveyed navigational information. The authenticity and consistency result from the continuous monitor and control by the GNSS ground segment. Thus, all signal characteristics determined by the spatial feature should be consistent with the navigational information. As for our concern, the actual elevation of the satellite determines the Doppler-ripple measurement $\hat{\mathbf{F}}$. The consequent projection vector $\hat{\mathbf{u}}_1$ should be largely proportional to $\bar{\boldsymbol{\theta}}$, which can be formulated as follows:

$$\exists k \in \mathbb{R}, \text{ s.t. } \hat{\mathbf{u}}_1 \cong k\bar{\boldsymbol{\theta}} \quad (16)$$

However, the spoofing signal might break this proportionality in two levels. The first level is the spatial feature, namely the estimated projection vector $\hat{\mathbf{u}}_1$. Generally, all spoofing transmitters do not occupy the same position of the corresponding GNSS satellites and probably have different actual elevations. Thus, the Doppler ripple of the spoofing signal has relative amplitudes different than the authentic situations. Therefore, the projection vector estimated from the spoofing signal $\hat{\mathbf{u}}'_1$ is usually different from the authentic one. For those spoofing measures which do not change the ephemeris or the positioning result, the satellite elevations $\bar{\boldsymbol{\theta}}$ are conserved. Since $\bar{\boldsymbol{\theta}}$ is proportional to $\hat{\mathbf{u}}_1$ estimated from the authentic signals, it would not be proportional to $\hat{\mathbf{u}}'_1$ estimated from the spoofing signal

$$\forall k \in \mathbb{R}, \text{ s.t. } \hat{\mathbf{u}}'_1 \not\cong k\bar{\boldsymbol{\theta}} \quad (17)$$

The second level is the navigational information, i.e. the elevation sine vector $\bar{\boldsymbol{\theta}}$ in the scope of this paper. The satellite elevations might be changed, either because the ephemeris data is altered or the positioning result is dramatically changed. Therefore, the sine vector calculated from the spoofing signal $\bar{\boldsymbol{\theta}'}$ would also be different from the authentic one. Consequently, the projection vector estimated from the spoofing signal $\hat{\mathbf{u}}'_1$ would not be proportional to $\bar{\boldsymbol{\theta}'}$

$$\forall k \in \mathbb{R}, \text{ s.t. } \hat{\mathbf{u}}'_1 \not\cong k\bar{\boldsymbol{\theta}'} \quad (18)$$

Therefore, in summary, the proportionality between the projection vector estimated from the Doppler ripple and the elevation sine vector calculated from the traditional positioning process is sufficient to act as a spoofing indicator. The proportionality could be quantitatively described by the correlation coefficient between $\hat{\mathbf{u}}_1$ and $\bar{\boldsymbol{\theta}}$.

3.3 Proposed spoofing-detection method

However, each component in the estimated projection vector $\hat{\mathbf{u}}_1$ has different standard deviations, denoted as q_i . Thus, a more comprehensive metric of the proportionality between $\hat{\mathbf{u}}_1$ and $\bar{\boldsymbol{\theta}}$ is a weighted correlation coefficient like

$$\rho = \bar{\boldsymbol{\theta}}^T \mathbf{Q}^T \mathbf{Q} \hat{\mathbf{u}}_1 / \| \mathbf{Q} \bar{\boldsymbol{\theta}} \| \| \mathbf{Q} \hat{\mathbf{u}}_1 \| \quad (19)$$

where $\mathbf{Q} \propto \text{diag}[q_1^{-1}, q_2^{-1}, \dots, q_l^{-1}]$ is called the post-whitening matrix, which will be addressed in the next chapter.

In non-spoofing scenarios, ρ is typically very close to 1, making the test statistic less intuitive. We could use the minus logarithm of this correlation coefficient ρ as the detection statistic

$$\gamma = -\log_{10}(1 - \rho) \quad (20)$$

Thus, the spoofing-detection hypothesis test could be expressed as

$$\begin{aligned} H_0 : \gamma &> \gamma_{\text{th}} \\ H_1 : \gamma &< \gamma_{\text{th}} \end{aligned} \quad (21)$$

where H_0 stands for the non-spoofing situation, where the projection vector $\hat{\mathbf{u}}_1$ estimated from Doppler ripple is proportional to the sine value of the elevation calculated from the navigation solution $\bar{\boldsymbol{\theta}}$. H_1 indicates that the signal might be compromised by spoofing, making $\hat{\mathbf{u}}_1$ disproportional to $\bar{\boldsymbol{\theta}}$.

As shown in Fig. 1, the operational procedures of the proposed method could be summarised as the following steps:

- i. Track all GNSS signals, and estimate the pre-whitening matrix \mathbf{C} from the carrier-to-noise ratio.
- ii. Get navigation solution to acquire elevation sines vector $\bar{\boldsymbol{\theta}}$.
- iii. Make rapid vertical reciprocating motion \mathbf{v} and collect the raw Doppler data.
- iv. Mitigate the long-term shifts to emphasise the Doppler ripple, and form the measurement matrix $\hat{\mathbf{F}}$.
- v. Perform the noise whitening SVD to acquire the estimated projection vector $\hat{\mathbf{u}}_1$, along with the post-whitening matrix \mathbf{Q} .
- vi. Calculate the correlation coefficient ρ and the test statistic γ .
- vii. Compare γ with the predetermined threshold γ_{th} to make a detection verdict.

3.4 Remarks on the proposed method

The proposed detection method does not require the user to precisely control the antenna motion or measure the speed variation but rather only requires the antenna roughly moving along the vertical direction. Furthermore, unlike the horizontal motion, the vertical motion barely needs an external device for orientation, since the gravity of the Earth provides a clear and perceivable direction.

Moreover, the proposed detection method is capable of detecting the spoofing signals emitted from multiple antennas. As for single-antenna spoofing device, no matter what altitude the transmitter has, the resulting projection vector $\hat{\mathbf{u}}_1$ has an evenly distributed form, which obviously differs from the authentic situation characterised by the spatial diversity. Even for the distributed multi-antenna spoofer, if the actual elevation of each antenna is not equal to the one calculated from the spoofed navigation solution, the estimated $\hat{\mathbf{u}}_1$ would not be proportional to $\bar{\boldsymbol{\theta}}$.

The proposed method trades some antenna motions for the detection capability against multi-antenna spoofing techniques. The enhancement in the detection capability arises from the joint consideration of the signal feature and the navigation information. To actively circumvent the proposed method, the spoofer needs to coordinate the spoofing navigational information and the relative position of the spoofing transmitter, which is quite difficult and thus provides chances for spoofing detection of the proposed method.

4 Performance analysis

In this chapter, we identify and assess several contributing factors, which impact the detection performance of the proposed method. These factors could be conceptually categorised into two classes: the estimation performance and the motion deviations.

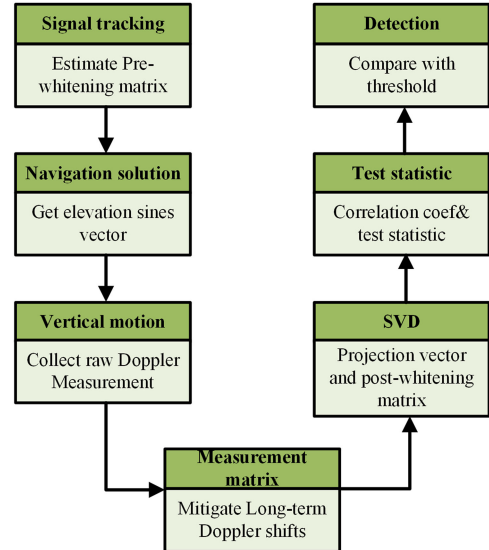


Fig. 1 Operational procedures

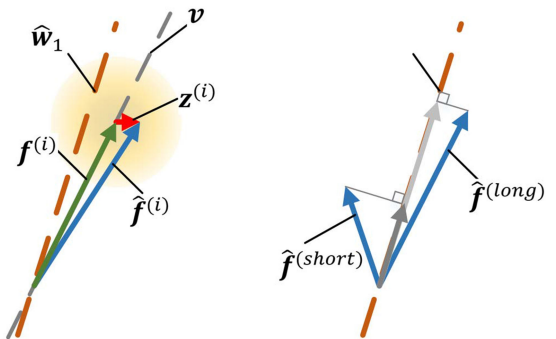


Fig. 2 Geometrical explanation

4.1 Estimation performance and Cramér–Rao bound

In this section, we first explain the noise impact on the SVD process from a geometrical perspective, then analyse the performance and the post-whitening matrix \mathbf{Q} .

From a geometrical perspective, the input of the SVD problem is the I Doppler-ripple measurement vectors $\hat{\mathbf{f}}^{(i)} \in \mathbb{R}^N$. Each $\hat{\mathbf{f}}^{(i)}$ could be deemed as the concatenation of two vectors: the noiseless Doppler-ripple vector $\mathbf{f}^{(i)}$ embedded in the actual speed vector \mathbf{v} subspace, and the noise vector $\mathbf{z}^{(i)}$, of which the ensemble can be modelled as a spheroid with a radius of δ_i . The pre-whitening procedure normalises these noise spheroids into the same size, while the noiseless vector $\mathbf{f}^{(i)}$ would be accordingly scaled by the whitening matrix \mathbf{C} . Therefore, the input vectors can be viewed as a vector with length $\frac{f_c \sin \theta_i}{c \delta_i} \parallel \mathbf{v} \parallel$ associated with a spherical arrowhead of radius 1. Each component of $\hat{\mathbf{u}}_1$ corresponds to the estimated relative projection length of the measurement vector $\hat{\mathbf{f}}^{(i)}$ onto the estimated subspace $\hat{\mathbf{w}}_1$. Generally, the estimated $\hat{\mathbf{w}}_1$ tends to be more parallel to the longer vector $\hat{\mathbf{f}}^{(\text{long})}$ with smaller noise, and more deviated from the shorter vector $\hat{\mathbf{f}}^{(\text{short})}$ with a larger noise. This tendency would make the estimation of $\hat{\mathbf{u}}_1$ a biased one, as illustrated in Fig. 2. Usually, the projected length of the shorter vector is more shrunk because of the angle is larger. The angle between the vector and the estimated subspace diminishes as the overall length grows, which alleviates the biasedness of the estimation. Practically, the Doppler ripple caused by 2 m/s speed would meet the unbiased condition.

As derived in the Appendix, the Cramér–Rao bound (CRB) for the projection vector $\hat{\mathbf{u}}_1$ and the speed vector $\hat{\mathbf{w}}_1$ follows:

$$\text{CRB}(\hat{\mathbf{u}}_1, \hat{\mathbf{w}}_1) = \mathbf{J}\mathbf{A}^+\mathbf{J}^T \quad (22)$$

where \mathbf{J} is the Jacobian matrix of relevant parameters and \mathbf{A} is the Fisher information matrix (FIM) of the original problem. Both \mathbf{J} and \mathbf{A} are determined by the actual elevation sines of the signal sources $\boldsymbol{\theta}$, the antenna motion speed \mathbf{v} , the number of signal channels I , the observation duration N and the Doppler measurement noise. However, in practise, the source elevation $\boldsymbol{\theta}$ and the Doppler noise are determined by the signal sources (either the GPS constellation or the spoofing transmitter) and the receiver hardware performance. We can only actively control the other three parameters, which are investigated in the next simulation.

Fig. 3 shows the estimation error and the CRB versus several tunable parameters such as the overall amplitudes determined by the maximum speed, the number of visible satellites and the observation duration. For visual clarity, only one out of the involved satellites is shown since the trend is similar for all components. Thus, as the maximum speed increases the Doppler-ripple amplitudes, the estimation accuracy of the projection vector $\hat{\mathbf{u}}_1$ asymptotically approaches the CRB, and the pre-whitening technique boosts this process because it promotes the estimation accuracy of the subspace $\hat{\mathbf{w}}_1$. The increase of the number of the visible satellites usually promotes the estimation of $\hat{\mathbf{w}}_1$, which in turn decreases the error variance of each component in $\hat{\mathbf{u}}_1$. Longer observation duration also benefits estimation performance.

Although all components in the projection vector $\hat{\mathbf{u}}_1$ have the same tendency versus relevant parameters, each of them has different accuracy within the same configuration. The CRB presented in (22) and the Appendix predicts the variance of each component in $\hat{\mathbf{u}}_1$. Fig. 4 shows the noise level, estimation mean and standard deviation of each satellite. As shown in Fig. 4, the estimation means are consistent with the true values, and the simulated outcomes are coherent to the CRB prediction.

Nonetheless, these heterogeneous precisions hinder the calculation of the correlation coefficient, it could be mitigated by the post-whitening matrix \mathbf{Q} as shown in (19). Moreover, this weighting matrix does not necessarily reflect the actual variance of each component in $\hat{\mathbf{u}}_1$ but rather only needs to be proportional to them. A quick but considerably precise method to calculate \mathbf{Q} is part of the Jacobian matrix

$$\mathbf{Q} = \mathbf{J}_u (\mathbf{C}^T \mathbf{C})^{-1} \mathbf{J}_u^T \quad (23)$$

where \mathbf{C} is the pre-whitening matrix in (15), \mathbf{J}_u is part of the Jacobian matrix \mathbf{J} in (22). The detailed calculation of \mathbf{Q} is included in the Appendix.

Another Monte Carlo simulation is carried out to verify these noise whitening techniques.

Fig. 5 shows the comparison among the statistic distributions with Doppler-ripple amplitudes from 2.5 up to 10 Hz. As we see that the pre-whitening SVD provides a considerable edge in the low signal-to-noise ratio situations, while the margin shrinks with increasing amplitudes. The post-whitening technique contributes a stable and obvious boost. Therefore, the bi-whitening SVD, which combines the pre-whitening and the post-whitening techniques, achieves the optimal performance.

Summarily, the estimation performance is determined by the observation time, Doppler measurements precision and antenna speed. If the Doppler-ripple amplitudes are much larger than the carrier loop precision δ_i , the CRB applies. If the number of Doppler-ripple snapshots is much larger than the number of visible satellites, the simplified calculation of post-whitening matrix \mathbf{Q} comes into effect.

So far, the estimation performance has already been addressed; we will now investigate the detection performance. However, in spoofing scenarios, $\hat{\mathbf{u}}_1$ is determined by the spoofing receiver geometry and $\hat{\boldsymbol{\theta}}$ is derived from the spoofing signals. We cannot enumerate all possible spoofing strategies to get the universal distribution of test statistic γ . Therefore, we cannot theoretically determine the detection performance in a closed-form expression.

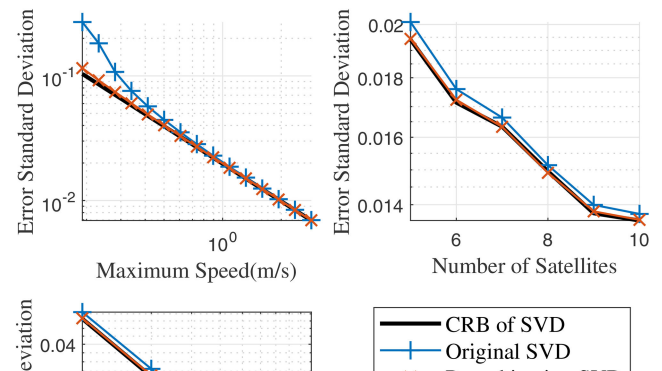


Fig. 3 Error in $\hat{\mathbf{u}}_1$ versus several parameters

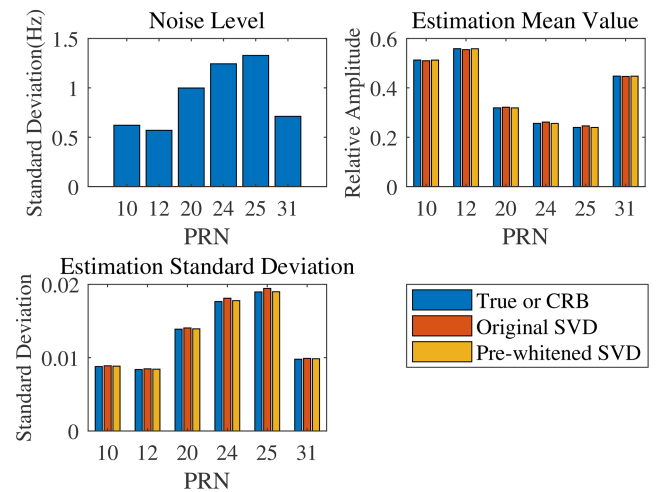


Fig. 4 Estimation performance of different satellites

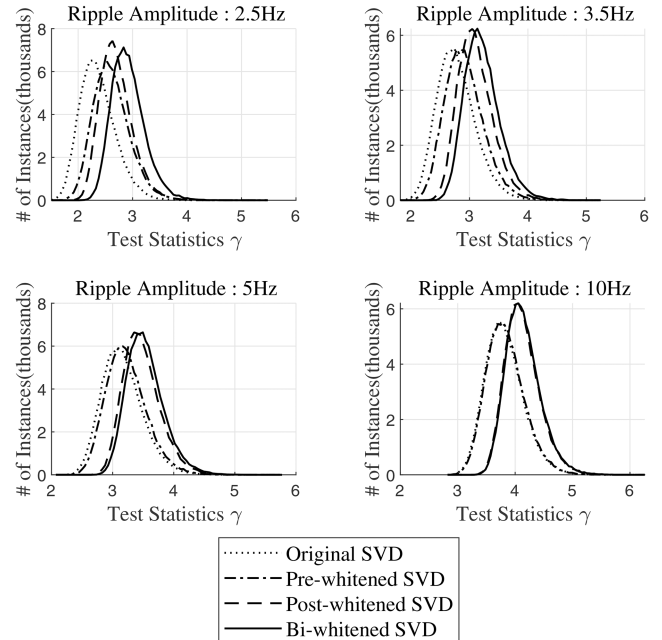


Fig. 5 Statistic distributions of different techniques with varying amplitudes

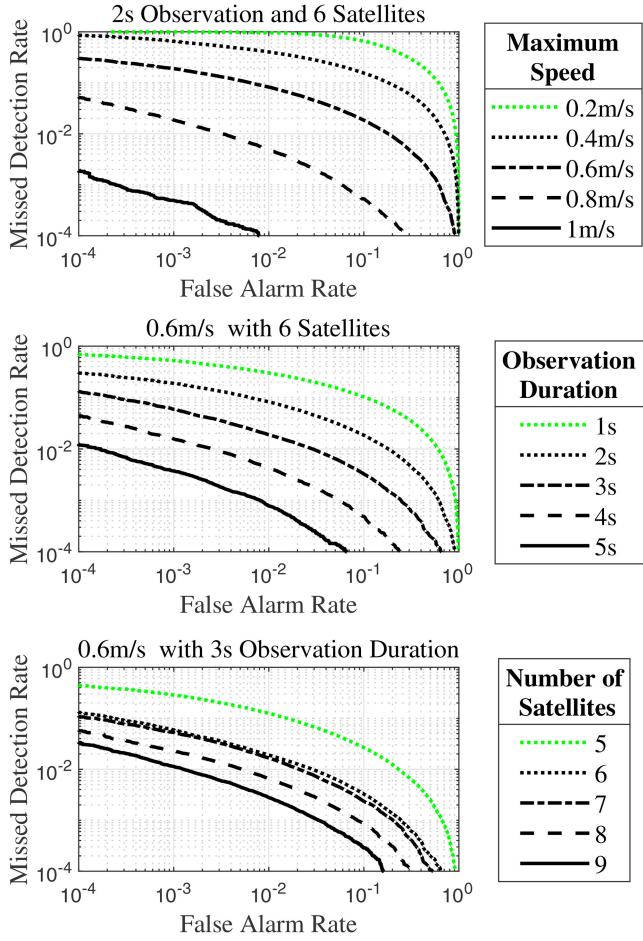


Fig. 6 Simulation results versus various parameters

However, if we focus on a specific spoofing strategy, the detection performance can be investigated by simulation. Each panel in Fig. 6 depicts the detection performance impact of one specific parameter. The simulated spoofing strategy is single-antenna spoofing, and the elevations derived from the spoofing signal are still the same as its authentic counterpart.

Qualitatively speaking, since higher antenna speed, longer observation duration and more satellites improve the estimation accuracy, leading to higher test statistics in non-spoofing scenarios, thus the threshold γ_{th} determined by Neyman–Pearson lemma could be larger. Larger threshold makes the missed detection less likely to happen and finally improves the detection performance.

4.2 Motion deviation

As the method requires, the ideal motion pattern is to make the receiving antenna move along the vertical axis in a straight line. Deviation from this ideal motion pattern might break the projection vector $\hat{\mathbf{u}}_1$ and the elevation sines $\hat{\theta}$ even without spoofing signal, leading to a false alarm and thus deteriorates the detection performance. These deviations could be roughly categorised into two different types: the non-linearity in the antenna motion and the vertical direction inaccuracy.

4.2.1 Motion non-linearity: Linear motion is not costless, and non-linear motion is inevitable. If the trail of the antenna motion is not a straight line but a curvy or twisted one, the rank of corresponding Doppler-ripple measurement matrix would be changed to two or even three.

Consequently, the outcome of the SVD process would be different from the one of the linear motions. The consequent submaximal singular values would be greatly elevated. As for the singular vectors, the first r right singular vectors constitute the orthonormal base in the row space of the consequent measurement matrix, which would probably not be parallel to the physically

meaningful subspaces. As we demonstrate in experiments, the non-linear motion pattern would significantly raise the false alarm rate.

However, there is one type of non-linear motion that is acceptable. This motion pattern is quite common in the marine scenarios, where ships moving on the water surface are influenced by the continuing water waves. Therefore, the uniform linear motion of the ship is usually associated with a vertical reciprocating motion because of the water wave [19]. The resultant Doppler variation caused by the translational motion is not volatile as the one caused by vertical reciprocating motion. Thus, the averaging process eliminates the long-term Doppler shift, leaving the Doppler-ripple undamped.

4.2.2 Vertical direction inaccuracy: Even if the antenna could strictly move in a straight line, we still need to keep the line parallel to the vertical axis (i.e. the up axis in local ENU coordinate system) to ensure that the projection vector $\hat{\mathbf{u}}_1$ is proportional to the elevation sines $\hat{\theta}$.

If the trajectory is not vertical, the tilted linear reciprocating motion makes the elevation ‘in effect’ differ from the elevation derived from the navigation solution. The exact change of the elevation ‘in effect’ depends on both the geometry and the axis tilt. Geometrically, the axis tilt could be described by two parameters, namely the pitch angle η and the yaw angle ψ . Thus, the elevation ‘in effect’ of a satellite with actual elevation θ_i and azimuth φ_i would be changed to

$$\theta'_i = \theta_i + \eta \cos(\psi - \varphi_i) \quad (24)$$

Therefore, for a specific tilt, the recovered projection vector $\hat{\mathbf{u}}_1$ would be unparalleled to the navigation elevations $\hat{\theta}$. This would increase the false alarm rate considerably. In this paper, we hold the receiving antenna in hand and keep the trajectory vertical by sensing the gravity, which presents the local vertical direction precisely. Normally, the perception error of gravity direction by human visual and vestibular sensation is usually $<5^\circ$ [20], which is more than acceptable as shown in the next chapter.

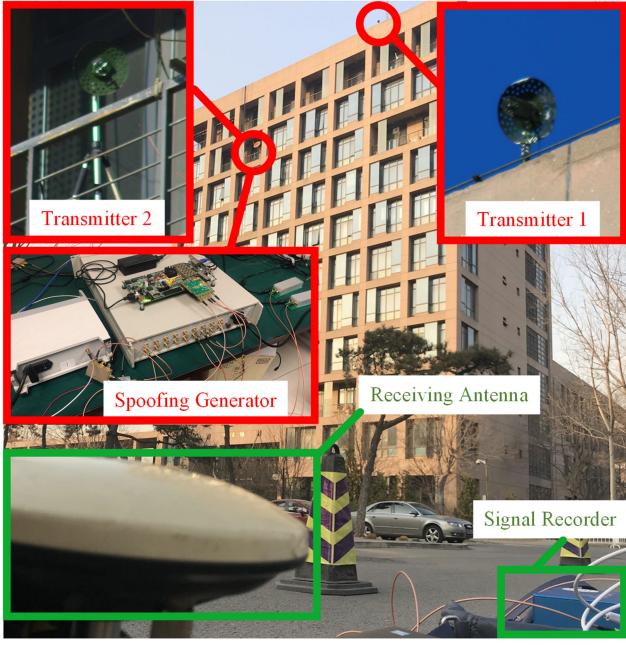
5 Experimental results

We have conducted a series of experiments to verify the effectiveness and evaluate the detection performance of the proposed method.

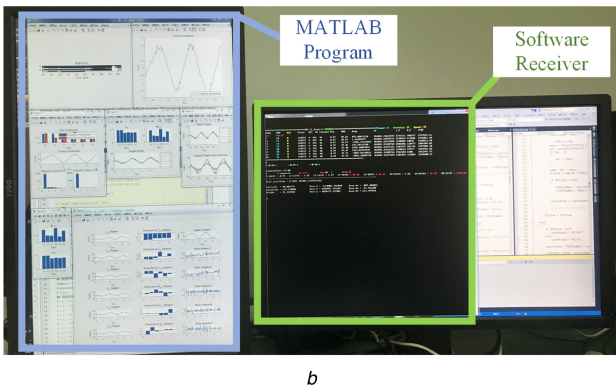
5.1 Experimental settings

Fig. 7a depicts the spoofing scenario we construct. The spoofing signal is generated by a receiver–spoofe which emulates the one invented by [1]. The single-antenna spoofing configuration is achieved by transmitting the spoofing signal through only one antenna, which is located at the top of the 11-story Weiqing Building at Tsinghua University, Beijing, China. The multi-antenna spoofing strategy deploys two transmitting antennas, of which the additional antenna is located at the balcony on the tenth floor. The signal is collected by a hand-held antenna and a signal recorder and then processed by software-defined receiver shown in Fig. 7b. The SVD process is carried out on $\hat{\mathbf{F}}$ in post-processing to estimate both the projection vector $\hat{\mathbf{u}}_1$ and the speed vector $\hat{\mathbf{w}}$.

We carry out the required vertical reciprocating motion by holding the receiving antenna in hand and making squats while keeping the trail of the antenna along the vertical axis. Fig. 8 includes all motion patterns involved in our experiment to validate the proposed method and the pertaining analysis. The pattern A is the regular vertical reciprocating motion we deem as the orthodox, whereas patterns B and C demonstrate two common irregular motion patterns pointed out in the previous chapter, namely the gravity direction tilt and non-linear motion. Pattern D emulates the motion patterns of a yacht or a boat moving at a constant speed while fluctuating on the waves.



a



b

Fig. 7 Experimentation devices and configuration
(a) Experiment configuration, (b) Signal processing devices

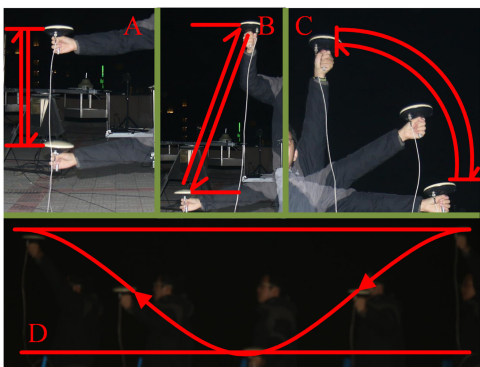


Fig. 8 Antenna motion patterns applied in experiments

5.2 Detection effectiveness verification

The first set of experiments aims to verify the effectiveness of both non-spoofing and spoofing situations. Fig. 9 shows the experimental results under the non-spoofing scenario including the output projection vector \hat{u}_1 and its comparison with the elevation sines $\bar{\theta}$ from navigation and the estimated speed vector \hat{w}_1 . The vertical reciprocation has a period of 2 s; the maximum speed is about 3 m/s; and the distance between the highest and lowest points is about 1 m. It could be seen that the proposed method works properly in the authentic signal environment. This result practically validates the consistency between Doppler ripple and the navigational solution in non-spoofing scenarios.

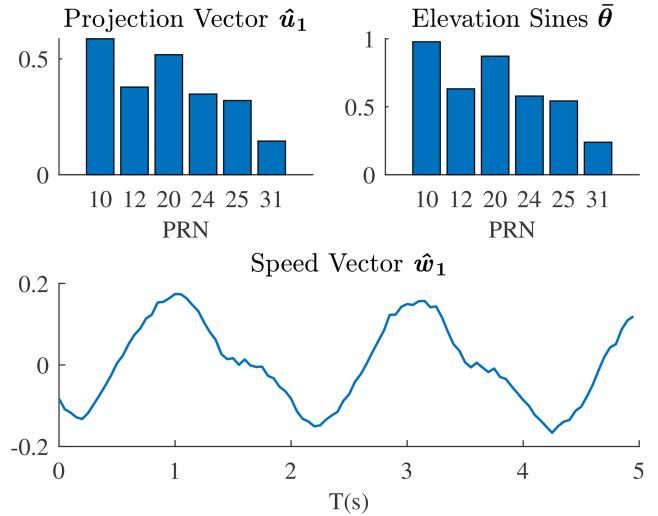


Fig. 9 Projection vector, speed vector and sine value of elevation in the non-spoofing scenario

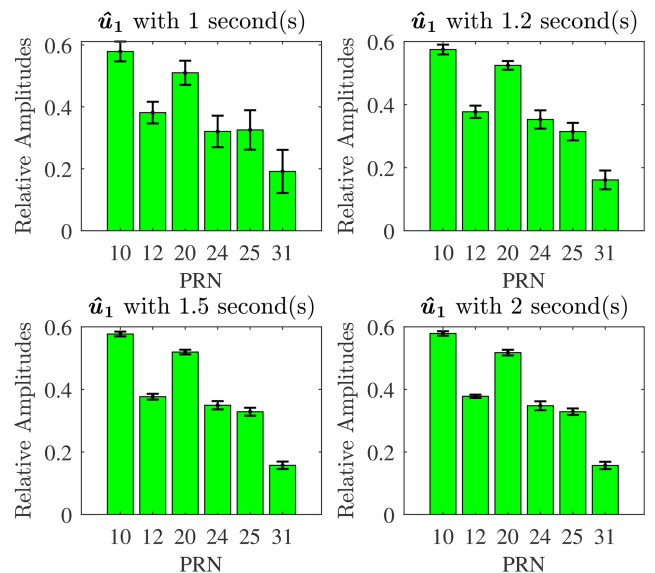


Fig. 10 SVD outcomes with various observation durations

Fig. 10 depicts the estimated \hat{u}_1 and variances with various observation durations. As seen, even with 1 s Doppler measurement, \hat{u}_1 still resembles $\bar{\theta}$ shown in Fig. 9. However, \hat{u}_1 with shorter observation is less precise, corroborating with the theoretical and simulation analyses.

As for the outcomes with 1.2 and 1.5 s, \hat{u}_1 is still largely proportional to $\bar{\theta}$ shown in Fig. 9. Thus, it could be said that the proposed method does not require synchronisation between the movement and the observation duration.

Fig. 11 depicts the output projection vector \hat{u}_1 and the elevation sines $\bar{\theta}$ in single- and double-antenna spoofing scenarios. Hereby, the deployed spoofing signals preserve the authentic ephemeris, and the positioning solution derived from the spoofing signal is about 100 m away from the authentic position. Note that since the Doppler frequency fluctuation is determined by the actual transmitter-receiver geometry; therefore, even the spoofed position is the same as the actual one, their relative amplitudes \hat{u}_1 would still be different from the elevation sines derived from the spoofing signals. Thus, the calculated satellite elevations $\hat{\theta}$ are equal to the authentic counterpart θ , while the actual position of the spoofing antennas as shown in Fig. 7a shows different than the satellites, making the estimated projection vector \hat{u}_1 disproportional to $\bar{\theta}$. Therefore, the corresponding test statistics γ are 1.25 and 1.16, whereas the non-spoofed statistic in Fig. 9 is 4.11, indicating that

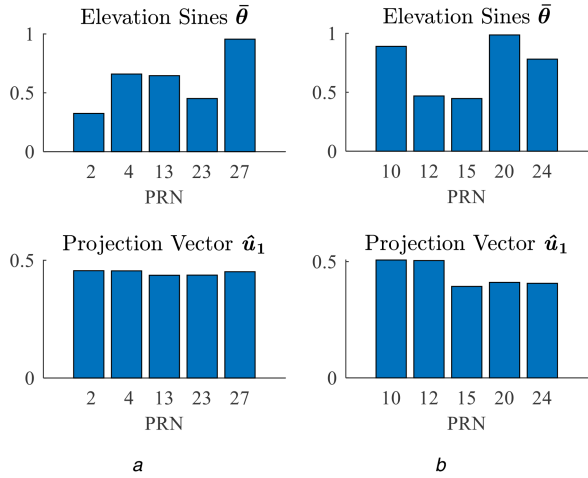


Fig. 11 Comparison between \hat{u}_1 and $\bar{\theta}$ in single- and multi-antenna spoofing scenarios

(a) Single-antenna spoofing, (b) Double-antenna spoofing

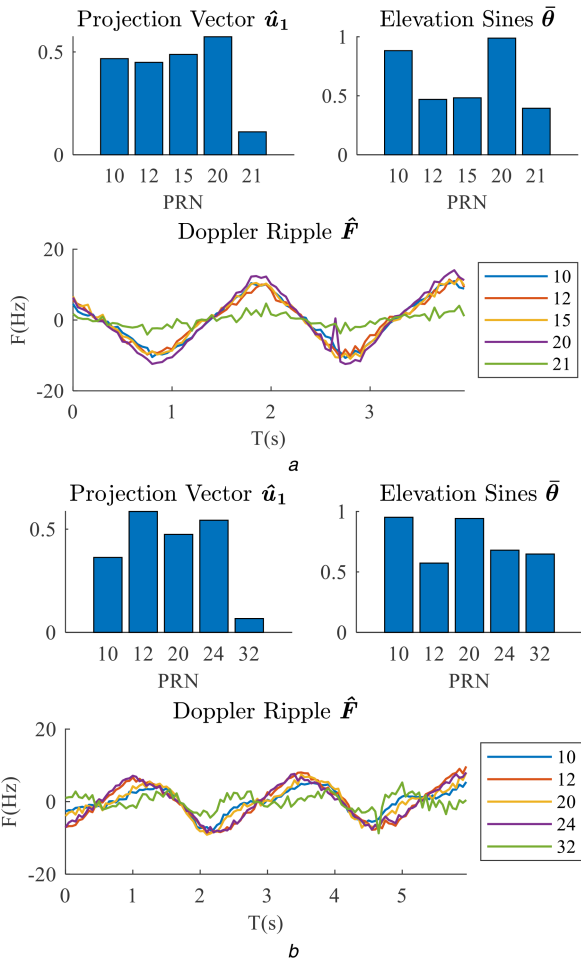


Fig. 12 Projection vector, elevation sines and Doppler ripple with motion deviation in non-spoofing scenarios

(a) Vertical direction inaccuracy, (b) Motion non-linearity

the proposed method could surely detect the spoofing signals from both single-antenna and multi-antenna spoofing devices.

The results in this section demonstrate the detection effectiveness of the proposed method against spoofing signals from one or two transmitters on the hand-held receiving antenna.

5.3 Motion deviation validation

In this section, we will practically validate the impact of motion deviations as discussed in the previous chapter. Fig. 12 shows the

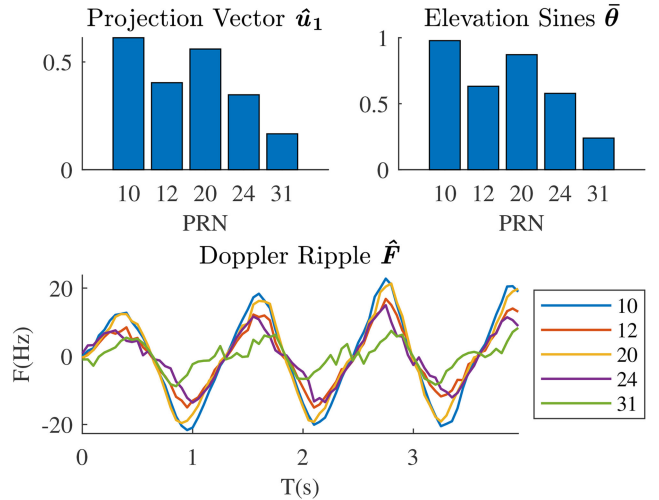


Fig. 13 Outcome from mobile non-spoofing scenarios

resultant Doppler ripple and SVD outcomes to exemplify the motion irregularities' effect in non-spoofing scenarios as discussed in the previous chapter, namely the gravity direction inaccuracy and non-linear motion.

The result of motion pattern B in Fig. 8 is shown in Fig. 12a. The pattern of the Doppler ripple is similar to the required one, whereas the estimated projection vector \hat{u}_1 obviously disagrees with $\bar{\theta}$, which is derived from the authentic signal. This is because the motion axis is not vertical due to the inaccurate gravity orientation. Fig. 12b illustrates the result of a non-linear motion similar to pattern C in Fig. 8, which significantly changes the shape of the Doppler ripple. The non-linear motion introduces a second Doppler change mode, which spans a second linear space in the row space of Doppler-ripple measurement matrix. Therefore, as previously discussed, the estimated projection vector \hat{u}_1 inevitably becomes no more parallel to $\bar{\theta}$, leading to a false alarm. These experiments validate that motion irregularities cause performance deterioration. However, the success as shown in Fig. 9, also proves that these deviated motion patterns can be easily avoided in practise.

The acceptable non-linear motion pattern is also validated. Fig. 13 shows the mobile situation in non-spoofing scenarios. The antenna is mounted on a uniformly translating vehicle, while still making the vertical reciprocating motion. Therefore, this experiment proves that the proposed method is also applicable to these vehicular scenarios.

This section demonstrates that the proposed method is not only useful in pedestrian scenarios but also applicable to the receiver fixed on a boat or ship.

5.4 Detection comparison with previous methods

To fully understand the advantages in detection capability, we also conduct several comparative experiments in the dual spoofing antenna configurations as shown in Fig. 7a. Each antenna transmits four different spoofing signals to the receiving antenna, which moves in the pattern according to the corresponding detection method. Fig. 14 shows the results from two precedent methods as we mention in the first chapter [11, 14].

Fig. 14a shows the results of the channel gain correlation monitor method proposed in [11] including the amplitude variation of the different signal as the input data and the correlation matrix as the test statistics. The amplitude variations of the signals bearing Pseudo Random Number (PRN) 14, 20, 24, 31 from the spoofing transmitter 1 are clearly correlated with each other, while the other four from transmitter 2 are highly correlated with each other. The signals from different spoofing transmitters are barely correlated with each other. Since the propagation paths from transmitters 1 and 2 are different, thus the different propagation gain variations are scarcely correlated. This outcome is consistent with the limitation of the single-antenna presumption in this method, validating that the method in [11] is ineffective against the multi-

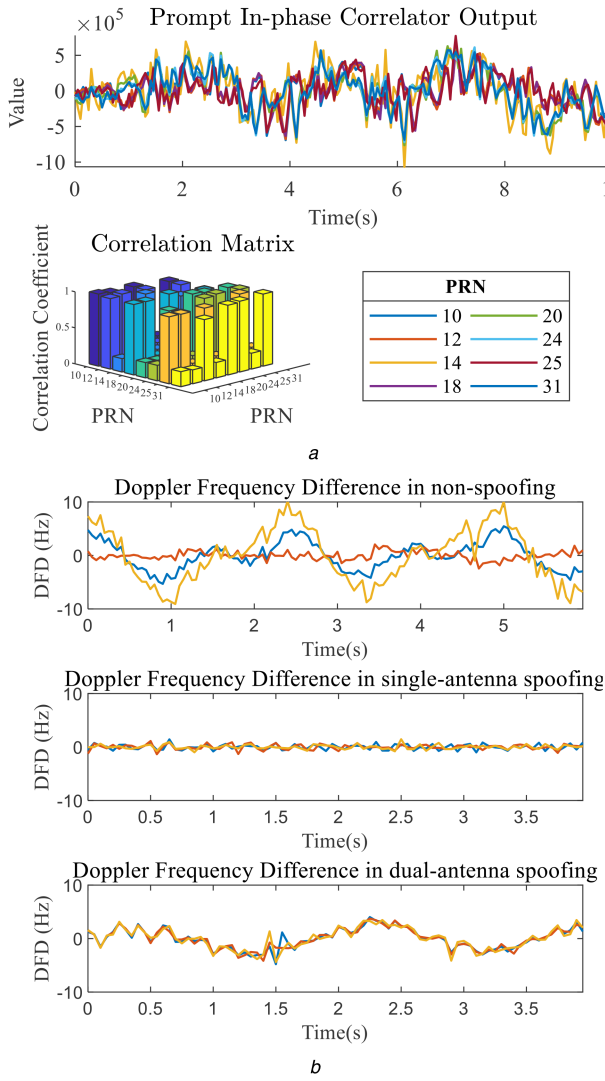


Fig. 14 Various precedent methods against dual-antenna spoofing configuration

(a) Channel gain correlation monitor method, (b) DFD method

antenna spoofing strategy [21], in which one spoofing transmitter emits only one specific spoofing signal.

Fig. 14b depicts the DFD measurement as a spoofing-detection indicator [14] including three different situations, namely the authentic, the single-antenna spoofing and the dual-antenna spoofing. Only four signals are chosen and processed for brevity and comparability among different situations. Just as [14] points out, the DFD measurement between signals is not linear in authentic scenarios, while the DFD is basically linear in the single-antenna spoofing scenarios. However, the DFD measurement in dual-antenna spoofing experiment behaves much more similar to the authentic situation than the single-antenna spoofing ones. What could be expected that the DFD monitor method would be more insufficient against the multi-antenna spoofing strategy [21].

The experimental evidence shown in Figs. 9, 11 and 14 adds up to one conclusion: to deal with the dual-antenna spoofing technique, the spoofing-detection method proposed in this paper is more effective than the precedent works. Moreover, the proposed method is also very likely effective against the multi-antenna spoofing strategy in [21]. This corroborates the discussion in the previous chapters.

6 Conclusion

In this paper, we propose a spoofing-detection method, which jointly utilises the navigational information conveyed by the GNSS signal and the ripple-like Doppler variation induced by the vertical reciprocating motion of a receiver. Through accumulating the measurement matrix and SVD-based algorithm, we could check the

congruence between the estimated projection vectors with the sine value of the satellite elevation. The authentic signal has the consistency between signal characteristics and the navigational information, while the spoofing signal and device cannot preserve this consistency.

We also thoroughly investigate the impact factors on the detection performance, along with other practical aspects. The experimental results provided hereby prove the effectiveness and validity of the proposed method. It could be concluded that our method is both effective and economical for spoofing-detection purpose in areas such as hand-held terminals and marine vehicles. This method does not require any mechanical direction pointer, since the local gravity field not only provides perceivable vertical axis in hand-held scenarios but also spurs up-and-down fluctuation of the marine vehicles.

The proposed method only requires the receiver antenna moving up and down along the vertical axis for no more than several seconds. It could not only detect the spoofing signal from single-antennaspoof but also could tackle with the multi-antennaspooftchniques. Only when the spoofing device has proper relative altitude and could also coordinate the ‘alleged’ navigational information, the proposed method could be circumvented. However, this significantly increases the cost and complexity of the spoofing attack.

7 Acknowledgments

This work was supported by the National Natural Science Foundation of China (Grant no. 61571255) and the Tsinghua University Initiative Scientific Research Program (Grant no. 2018Z05JZY004).

8 References

- [1] Humphreys, T.E., Ledvina, B.M., Psiaki, M.L., *et al.*: ‘Assessing the spoofing threat: development of a portable GPS civilianspoof’. Proc. ION GNSS Int. Technical Meeting of the Satellite Division, Savannah, GA, USA, September 2008, pp. 2314–2325
- [2] Psiaki, M.L., Humphreys, T.E.: ‘GNSS spoofing and detection’, *Proc. IEEE*, 2016, **104**, (6), pp. 1258–1270
- [3] Kerns, A.J., Wesson, K.D., Humphreys, T.E.: ‘A blueprint for civil GPS navigation message authentication’. IEEE/ION-PLANS Position, Location and Navigation Symp., Monterey, CA, USA, May 2014, pp. 262–269
- [4] Scott, L.: ‘Anti-spoofing & authenticated signal architectures for civil navigation systems’. Proc. 16th Int. Technical Meeting of the Satellite Division of The Institute of Navigation (ION GPS/GNSS 2003), Portland, OR, USA, September 2001, pp. 1543–1552
- [5] Tanil, C., Khanafseh, S., Joerger, M., *et al.*: ‘An INS monitor to detect GNSS spoofers capable of tracking vehicle position’, *IEEE Trans. Aerosp. Electron. Syst.*, 2018, **54**, (1), pp. 131–143
- [6] Vagle, N., Broumandan, A., Lachapelle, G.: ‘Multiantenna GNSS and inertial sensors/odometer coupling for robust vehicular navigation’, *IEEE Internet Things J.*, 2018, **5**, (6), pp. 4816–4828
- [7] Seo, S-H., Lee, B-H., Im, S-H., *et al.*: ‘Efficient spoofing identification using baseline vector information of multiple receivers’, *GPS Solut.*, 2018, **22**, (4), p. 115
- [8] Psiaki, M.L., O’Hanlon, B.W., Bhatti, J.A., *et al.*: ‘GPS spoofing detection via dual-receiver correlation of military signals’, *IEEE Trans. Aerosp. Electron. Syst.*, 2013, **49**, (4), pp. 2250–2267
- [9] Borio, D., Gioia, C.: ‘A sum-of-squares approach to GNSS spoofing detection’, *IEEE Trans. Aerosp. Electron. Syst.*, 2016, **52**, (4), pp. 1756–1768
- [10] Psiaki, M.L., O’hanlon, B.W., Powell, S.P., *et al.*: ‘GNSS spoofing detection using two-antenna differential carrier phase’. Proc. ION GNSS + 2014, Tampa, FL, USA, September 2014, pp. 2776–2800
- [11] Broumandan, A., Jafarnia-Jahromi, A., Dehghanian, V., *et al.*: ‘GNSS spoofing detection in handheld receivers based on signal spatial correlation’. IEEE/ION Position Location and Navigation Symp. (PLANS), Myrtle Beach, SC, USA, April 2012, pp. 479–487
- [12] Psiaki, M.L., Powell, S.P., O’hanlon, B.W.: ‘GNSS ‘spoofing detection using high-frequency antenna motion and carrier-phase data’. Proc. ION GNSS + Meeting, Nashville, TN, USA, September 2013, pp. 2949–2991
- [13] Wang, F., Li, H., Lu, M.: ‘GNSS spoofing countermeasure with a single rotating antenna’, *IEEE Access*, 2017, **5**, pp. 8039–8047
- [14] Tu, J., Zhan, X., Zhang, X., *et al.*: ‘Low-complexity GNSS anti-spoofing technique based on Doppler frequency difference monitoring’, *IET Radar Sonar Navig.*, 2018, **12**, (9), pp. 1058–1065
- [15] De Moor, B.: ‘The singular value decomposition and long and short spaces of noisy matrices’, *IEEE Trans. Signal Process.*, 1993, **41**, (9), pp. 2826–2838
- [16] Edfors, O., Sandell, M., Van de Beek, J-J., *et al.*: ‘OFDM channel estimation by singular value decomposition’, *IEEE Trans. Commun.*, 1998, **46**, (7), pp. 931–939
- [17] Raychev, N.: ‘Measure of entanglement by singular value decomposition’, *Int. J. Sci. Eng. Res.*, 2015, **6**, (7), pp. 1350–1355

- [18] Kaplan, E., Hegarty, C.: ‘Understanding GPS: principles and applications’ (Artech House, Norwood, MA, USA, 2005, 3rd edn.), pp. 482–486
- [19] Salvesen, N., Tuck, E., Faltinsen, O.: ‘Ship motions and sea loads’, *Trans. Soc. Naval Archit. Mar. Eng.*, 1970, **78**, (8), pp. 250–287
- [20] Schone, H.: ‘On the role of gravity in human spatial orientation’, *Aerospace Med.*, 1964, **75**, pp. 764–772
- [21] Tippenhauer, N.O., Popper, C., Rasmussen, K.B., et al.: ‘On the requirements for successful GPS spoofing attacks’. Proc. 18th ACM Conf. Computer and Communications Security, Chicago, IL, USA, October 2011, pp. 75–86
- [22] Kay, S.M.: ‘Fundamentals of statistical signal processing volume 1: estimation theory’ (Prentice-Hall PTR, America, 1993, 1st edn.)

9 Appendix

Reformulate the model of the Doppler ripple into a bilinear model by defining $s_i \triangleq \frac{f_c}{c} \sin \theta_i$

$$f_{\text{in}} = f_u^{(i)}[n] = s_i v_n + z^{(i)}[n] \quad (25)$$

where $z_{\text{in}} = z^{(i)}[n]$ obeys a zero-mean Gaussian distribution with variance δ_i^2 , all s_i and v_n are regarded as the unknown parameters. We denote the observation matrix $\hat{\mathbf{F}}$ and the unknown parameters as

$$\hat{\mathbf{F}} = \mathbf{s}\mathbf{v}^T + \mathbf{Z} \quad (26)$$

where $\mathbf{s} = \left[\frac{f_c}{c} \sin \theta_1, \frac{f_c}{c} \sin \theta_2, \dots, \frac{f_c}{c} \sin \theta_I \right]^T$.

To facilitate further deduction, we first introduce one abbreviating variable $D \triangleq \sum_{i=1}^I s_i^2 / \delta_i^2$, which reflects the total signal-to-noise ratio of different channels.

Therefore, the first-order derivative of the log-likelihood function of the observation matrix $\hat{\mathbf{F}}$ is like

$$\frac{\partial \ln p(\hat{\mathbf{F}}; \mathbf{s}, \mathbf{v})}{\partial s_i} = \frac{1}{\delta_i^2} \sum_{n=1}^N v_n (f_{\text{in}} - s_i v_n) \quad (27)$$

$$\frac{\partial \ln p(\hat{\mathbf{F}}; \mathbf{s}, \mathbf{v})}{\partial v_n} = \sum_{i=1}^I \frac{1}{\delta_i^2} s_i (f_{\text{in}} - s_i v_n) \quad (28)$$

Consequent second-order derivatives are like

$$\frac{\partial^2 \ln p(\hat{\mathbf{F}}; \mathbf{s}, \mathbf{v})}{\partial s_i^2} = -\frac{1}{\delta_i^2} \sum_{n=1}^N v_n^2 = -\frac{1}{\delta_i^2} \|\mathbf{v}\|^2 \quad (29)$$

$$\frac{\partial^2 \ln p(\hat{\mathbf{F}}; \mathbf{s}, \mathbf{v})}{\partial v_n^2} = -\sum_{i=1}^I \frac{s_i^2}{\delta_i^2} = -D \quad (30)$$

$$\frac{\partial^2 \ln p(\hat{\mathbf{F}}; \mathbf{s}, \mathbf{v})}{\partial s_i \partial s_j} = \frac{\partial^2 \ln p(\hat{\mathbf{F}}; \mathbf{s}, \mathbf{v})}{\partial v_n \partial v_m} = 0 \quad (31)$$

$$\frac{\partial^2 \ln p(\hat{\mathbf{F}}; \mathbf{s}, \mathbf{v})}{\partial s_i \partial v_n} = \frac{1}{\delta_i^2} (f_{\text{in}} - 2s_i v_n) = \frac{\partial^2 \ln p(\hat{\mathbf{F}}; \mathbf{s}, \mathbf{v})}{\partial v_n \partial s_i} \quad (32)$$

Thus, the FIM is achieved as the expectation of minus two-order derivatives of a log-likelihood function, which clearly falls into a block matrix

$$\Lambda(\mathbf{s}, \mathbf{v}) = \begin{bmatrix} \mathbf{A} & \mathbf{X} \\ \mathbf{X}^T & \mathbf{D} \end{bmatrix} \quad (33)$$

where \mathbf{A} , \mathbf{D} and \mathbf{X} are, respectively, formulated as

$$\mathbf{A} = \|\mathbf{v}\|^2 \text{diag} \left[\frac{1}{\delta_1^2} \quad \frac{1}{\delta_2^2} \quad \cdots \quad \frac{1}{\delta_I^2} \right] \quad (34)$$

$$\mathbf{D} = \mathbf{D}\mathbf{I}_N \quad (35)$$

$$\mathbf{X} = \begin{bmatrix} \frac{s_1 v_1}{\delta_1^2} & \frac{s_1 v_2}{\delta_1^2} & \cdots & \frac{s_1 v_N}{\delta_1^2} \\ \frac{s_2 v_1}{\delta_2^2} & \frac{s_2 v_2}{\delta_2^2} & \cdots & \frac{s_2 v_N}{\delta_2^2} \\ \cdots & \cdots & \cdots & \cdots \\ \frac{s_I v_1}{\delta_I^2} & \frac{s_I v_2}{\delta_I^2} & \cdots & \frac{s_I v_N}{\delta_I^2} \end{bmatrix} \quad (36)$$

Thus, the corresponding CRB matrix of this bilinear model is the Moore–Penrose inverse matrix of the FIM $\Lambda(\mathbf{s}, \mathbf{v})$

$$\text{CRB}(\mathbf{s}, \mathbf{v}) = \Lambda(\mathbf{s}, \mathbf{v})^+ \quad (37)$$

The underlying parameters of the SVD-based problem can be viewed as the functions of \mathbf{s} and \mathbf{v} . The first singular value σ_1 and the corresponding left and right singular vectors $\mathbf{u}_1, \mathbf{w}_1$ are expressed as $\sigma_1 = \mathbf{s}\mathbf{v}$, $\mathbf{u}_1 = \mathbf{s}/\mathbf{s}$ and $\mathbf{w}_1 = \mathbf{v}/\mathbf{v}$. Therefore, the Jacobian matrix $\mathbf{J}(\mathbf{s}, \mathbf{v})$ can be subsequently obtained [see (38)].

The CRB of the SVD results could be achieved through parameter transformation from the CRB of a bilinear model like [22]

(see (38))

$$\text{CRB}(\sigma_1, \mathbf{u}_1, \mathbf{w}_1) = \mathbf{J}(\mathbf{s}, \mathbf{v}) \Lambda(\mathbf{s}, \mathbf{v})^+ \mathbf{J}(\mathbf{s}, \mathbf{v}) \quad (39)$$

If the number of Doppler snapshots N is much larger than the number of visible satellites I , the upper-left part of the FIM would be dominant. Therefore, the Moore–Penrose inverse of the FIM $\Lambda(\mathbf{s}, \mathbf{v})^+$ would be basically determined by \mathbf{A} . Thus, for the interested projection vector $\hat{\mathbf{u}}_1$, the CRB can be approximated by the reduced form of the CRB of the SVD

$$\text{CRB}(\mathbf{u}_1) = \mathbf{J}_u \mathbf{A}^+ \mathbf{J}_u^T \quad (40)$$

where \mathbf{J}_u is a part of the Jacobian matrix $\mathbf{J}(\mathbf{s}, \mathbf{v})$, of which the entries only involve \mathbf{s} and \mathbf{u}_1

$$\mathbf{J}_u = \begin{bmatrix} \frac{S^2 - s_1^2}{S^3} & \cdots & -\frac{s_1 s_I}{S^3} \\ \cdots & \cdots & \cdots \\ -\frac{s_I s_1}{S^3} & \cdots & \frac{S^2 - s_I^2}{S^3} \end{bmatrix} \quad (41)$$

Since it is not possible to measure the speed vector, thus \mathbf{v} is not knowable. Therefore, the weighting matrix \mathbf{Q} could be calculated by the satellite elevations $\bar{\theta}_i$ from navigational information and the noise variance δ_i^2 estimated from the carrier-to-noise ratio

$$\mathbf{Q} = \mathbf{J}_u (\mathbf{C}^T \mathbf{C})^{-1} \mathbf{J}_u^T \quad (42)$$

where \mathbf{C} is the pre-whitening matrix reflecting the Doppler measurement noise.

$$J(\mathbf{s}, \mathbf{v}) = \begin{bmatrix} s_1 \frac{\|\mathbf{v}\|}{\|\mathbf{s}\|} & \dots & \frac{s_I \|\mathbf{v}\|}{\|\mathbf{s}\|} & \frac{v_1 \|\mathbf{s}\|}{\|\mathbf{v}\|} & \dots & \frac{v_N \|\mathbf{s}\|}{\|\mathbf{v}\|} \\ \frac{\|\mathbf{s}^2 - s_1^2}{\|\mathbf{s}\|^3} & \dots & -\frac{s_1 s_I}{\|\mathbf{s}\|^3} & 0 & \dots & 0 \\ \dots & \dots & \dots & \dots & \dots & \dots \\ -\frac{s_I s_1}{\|\mathbf{s}\|^3} & \dots & \frac{\|\mathbf{s}\|^2 - s_I^2}{\|\mathbf{s}\|^3} & 0 & \dots & 0 \\ 0 & \dots & 0 & \frac{\|\mathbf{v}\|^2 - v_1^2}{\|\mathbf{v}\|^3} & \dots & \frac{v_1 v_N}{\|\mathbf{v}\|^3} \\ \dots & \dots & \dots & \dots & \dots & \dots \\ 0 & \dots & 0 & -\frac{v_N v_1}{\|\mathbf{v}\|^3} & \dots & \frac{\|\mathbf{v}\|^2 - v_N^2}{\|\mathbf{v}\|^3} \end{bmatrix} \quad (38)$$